# Drying induced shrinkage of Boom Clay: an experimental investigation

Noémie Prime [1] [2]    Séverine Levasseur [1] [3]    Laurent Miny [1] [4]

Robert Charlier [1]    Angélique Léonard [5]    Frédéric Collin[1]

keywords : Drying, Boom Clay, shrinkage, hydro-mechanical coupling, tomography.

Drying induced shrinkage of geomaterials may have a strong effect on geostructure stability and deformation. Settlement of foundations, fracture opening on slopes, roads, tunnel walls may be due to drying shrinkage. However, there is still a lack of knowledge concerning shrinkage evolution in time and shrinkage propagation within the material. In this study, the shrinkage of a specific clayey rock, Boom Clay, under drying conditions is experimentally investigated. This rock is a deep geological formation which is under study for high-level and long-life radioactive waste storage in Belgium. Two experimental campaigns are here presented. The first one, based on vapour equilibrium drying technique and completed by sample size manual measurement, aims to characterize the material shrinkage in balanced states. The second one, based on convective drying technique completed by shape monitoring using X-ray tomography, aims to analyse how shrinkage develops before reaching a steady state. Both approaches put

[1]Université de Liège, dept. ArGEnCo, Liège, Belgium
[2]Now at Ecole Centrale Lyon, LTDS laboratory, Lyon, France; noemie.prime@gmail.com,noemie.prime@ec-lyon.fr
[3]Now at Ondraf-Niras, Belgian Agency for Radioactive Waste and Enriched Fissile materials, Brussels, Belgium
[4]Now at Greisch, Liège, Belgium
[5]Université de Liège, dept. Applied Chemistry, Liège, Belgium

1

19  in evidence the shrinkage anisotropy of this structurally bedded rock, with a ratio around 2

20  between the direction of maximum strains and the direction of minimum strains. However, the

21  two drying techniques also provide complementary results, as the relation between the amount

22  of shrinkage and the retention curve (for the uniform drying imposed with saline solutions) and

23  the kinetics of shrinkage propagation inside the material (for the non-uniform drying imposed

24  with air convection).

# 1  Introduction

Geomaterial drying is an important solicitation to deal with. On one hand, it is used as an industrial process for the production of some building materials as clay tiles or gypsum wallboards. In this context, it has to be controlled in order to be fast enough (for productivity need) but, in the same time, sufficiently slow and regular to prevent from cracking. On the other hand, drying also occurs under natural conditions for soils and rocks and, when followed by a wide number of drying-imbibition cycles, may damage the material. This happens for instance for building rock or concrete whose durability can be reduced due to cracks or to other marks of alteration (Alves et al. 1996; Granger 1995). For soils having a high sensitivity to water, drying induces shrinkage which can damage building structures by generating differential settlements (Nowamooz and Masrouri 2010), or can damage the sealing host rock considered for a potential underground nuclear waste storage (Gerard et al. 2008). Typically, expansive clays are concerned, as montmorillonite or smectite, for which the suction developed for non saturated state strains the solid matrix.

The interactions between the porous matrix, the liquid and the gaz phases being complex (they are ruled by thermodynamic, mechanical, hydraulic equilibrium), this problem remains a major scientific issue. Permanent strains induced in clay by drying are notably a wide and complex domain of investigation. They are linked to the change of clay mechanical behaviour under drying that becomes plastic and brittle, as experimentally highlighted by Musielak and Mierzwa (2009) by digital recording of video. As cracking causes direct damage of the clay (loss of mechanical resistance, increase of hydraulic conductivity), it is highly investigated with both experimental (Prime et al. 2014; Hedan et al. 2012; Banaszak and Kowalski 2005) and numerical approaches (Musielak and Sliwa 2013; Péron et al. 2009; Amarasiri et al. 2011). Shrinkage has also important consequences: not only because it permanently changes the material geometry and its mechanical properties, but also because a shrinkage gradient or a constrained shrinkage can cause the onset of cracking, that is to say a severe damage of the material (Peron et al. 2009). For this reason it has to be well characterized and predicted. In civil engineering great effort is made to catch this behaviour which is linked to the loss of saturation. Many experimental works thus aim to describe this soil volumetric response (Fleureau et al. 1993;

Tripathy et al. 2002) and many theoretical and numerical ones (Alonso et al. 1990; Loret and Khalili 2002; Kodikara 2012) aim to develop suitable models of behaviour. However, most of these approaches focus on the homogeneous and balanced response, in order to establish coupled hydro-mechanical laws. But the experimental response to a simple boundary condition applied, with both coupled behaviour and transient response is rarely presented, although it represents most of the drying mechanisms. Some works can however be mentioned: those by Léonard et al. (2002) which study sludges drying induced shrinkage by mean of X-ray tomography analysis or those by (Peron et al. 2009) which study the drying shrinkage of a fine grained soil and its associated cracking under non uniform mechanical and hydraulic conditions. Such experimental approaches can furnish important and complementary information to homogeneous response to drying, and it could be useful to validate unsaturated model of behaviour.

Within the scientific context above presented, this work aims to experimentally characterize drying induced shrinkage of a natural rock not only for balanced and uniform successive states but also for transient and non-uniform behaviour resulting from the set of a drying boundary condition. The main originality of the present work lays in this last analysis. The rock chosen for the study is Boom Clay, studied as a potential host rock for nuclear waste disposal into deep geological formations in Belgium. This storage project under study is based on a multi-barrier concept, in which the natural impermeable geological formation is the last confinement layer (Bernier et al. 2007) and therefore is largely investigated (Ortiz et al. 2002; Mertens et al. 2004; Bastiaens et al. 2007; Bernier et al. 2007; Chen et al. 2011). Drying is one of the host rock solicitations to study because it is expected in case of contact with the ambient atmosphere (during disposal drilling for instance) or during gallery ventilation (because of damage in lining of the main galleries). This present work thus also represents a valuable approach for the specific issue of nuclear waste underground storage.

This article is structured as follows. After a short description of Boom Clay particular features, a first experimental drying test is led with the objective to characterize shrinkage for uniform and equilibrated hydro-mechanical states obtained through vapour equilibrium technique. The second campaign goes beyond the study of this homogeneous response and

83   aims to analyse Boom Clay shrinkage evolution while equilibrium is not yet reached and hydro-

84   mechanical state not yet uniform. In this second campaign, drying is imposed by air convection

85   and  deformations are determined by tomography analysis. The results are processed in order

86   to get valuable information about the kinetics, the direction and the amount of shrinkage.

87   Lastly, a conclusion gathers the main results for each of these two approaches, compares both

88   of them and suggests some further directions of investigation concerning soft material drying.

## 2   Material studied

As previously stated, Boom Clay is a formation which is studied for the disposal, in Belgium, of high-level and long-life nuclear waste into deep geological formation. Researches have been done with the support of HADES (High Activity Disposal Experimental Site) Underground Research Laboratory (URL). It has been drilled in the 1980's in the Oligocen formation of Boom Clay at around 220 m below ground level. At such depth, the total pressure $p$ is about 4.5 MPa while the water pressure $u$ is about 2.25 MPa (the clay being saturated). Main material and hydric properties of this rock are gathered in table 1. For each parameter, this table presents the authors' estimations compared to classical ranges of variation that can be estimated from literature review. More specifically, all the clay samples analysed here originate from the core drilled in 2007 in the borehole referred to as "2007-3/Connecting Gallery / Ring 66-67E/Intrados". In the present study, dry density is determined with helium pycnometer technique, natural one is determined by paraffin covering and immersion, and porosity is deduced from the previous data and from the water content. The Atterberg limits have also been estimated here: the liquid limit equals 76% and the plastic limit equals 27%. It confirms that in its natural state ($w$=0.2-0.3), Boom Clay may undergo plastic strains, included during drying solicitations.

In addition, the layered structure of the formation, alternation of horizontal clay and silt layers, is responsible of a high anisotropy within the material. This internal structure is visible in figure 1 on a partially dried sample. Consequently, it exists a ratio closed to 2 between horizontal and vertical intrinsic permeabilities ($k_h$ and $k_v$ respectively), with $k_v \approx 2.10^{-19} \ m^2$ and $k_h \approx 4.10^{-19} \ m^2$, which can locally vary according to the nature of the layer (see Aertsens et al. (2004)).

6

*Table 1: Synthesis of material and hydraulic Boom Clay parameters. Literature data comes from Mertens et al. (2003); Dehandschutter et al. (2005); Bernier et al. (2007); Volckaert et al. (1996)*

|  |  |  | Literature | Experiment |  |
|---|---|---|---|---|---|
| Material parameters | $\rho_s$ | Grain density | 2650-2690 | 2610 | kg/m$^3$ |
|  | $\rho$ | Natural density | 1900-2100 | 2020 | kg/m$^3$ |
|  | $\phi$ | Porosity | 0.35-0.43 | 0.43 |  |
|  | $w_L$ | Liquid limit | 0.55-0.80 | 0.76 |  |
|  | $w_P$ | Plastic limit | 0.32-0.51- | 0.27 |  |
| Hydric parameters | $k$ | Intrinsic permeability | 2-4.10$^{-19}$ | - | m$^2$ |
|  | $w$ | In situ water content | 0.2-0.3 | 0.27 |  |
|  | $Sr$ | In situ degree of saturation | 100 | - | % |

# 3 Shrinkage analysis under vapour equilibrium drying

## 3.1 Experimental protocol

### 3.1.1 Principle of the experiment

In this approach, drying is applied by the transition of the material across successive hermetic chambers having decreasing relative humidities. In each chamber the air relative humidity is set by equilibrium with a specific over-saturated saline solution. It is the so called 'vapour equilibrium technique'.

The chamber relative humidity indirectly applies a fixed total suction to the clay since Kelvin equilibrium states that liquid water and water vapour in contact are in thermodynamical equilibrium. Total suction $s$ within the material and relative humidity $RH$ of the air are thus linked as follows:

$$RH = exp\left(\frac{sM_v}{RT\rho_w}\right), \tag{1}$$

with $M_v$ the molar mass of water and $R$ the universal gas constant. Decreasing the ambient relative humidity thus increases the suction $s$ within a porous medium, which corresponds to drying. The physical state of a cell being fixed and constant, water transfers take place, under a vapour form, between the atmosphere and the partially saturated clay samples. Water balance into the clay can be obtained after a certain time, and this state is expressed by a constant mass of the clay sample. More details about this technique, some of its developments and major drawbacks can be found in Tang and Cui (2005); Blatz et al. (2009).

Two series of drying tests, denoted A and B, are performed. Strains are only measured for series B. Series A contribute to check the Boom Clay retention curve along the drying path by comparison with literature results.

8

### 3.1.2  Sampling

30 cylindrical samples are drilled in Boom Clay from HADES Belgian laboratory with bedding planes being parallel to the cylinder axis. 15 of them are analysed through drying of series A (retention curve validation) whereas the other 15 are analysed through drying of series B (shrinkage analysis). All cylinders are approximately 30 mm high and 13 mm diameter. The saturated clay being very soft, the wet drilling for series B has to be slow enough in order to get a regular cylinder shape (more details on this procedure can be found in Miny 2013).

In the initial state, samples' mass and water content are determined. For samples of series B dimensions are also initially measured (with a slide caliper) and the bedding direction has to be marked in order to characterize the eventual anisotropy of the response. However, these planes are not visible when the clay is saturated but only appear during drying. Therefore, arbitrary direction is marked in each saturated sample with a thin cut at the top of the cylinder. Such marking is presented at figure 2. This arbitrary direction, along which the dimensions will be measured, has to be compared with the bedding planes' direction at the end of the test.

Clay samples are grouped in threes in order to have mean values of measuring when placed into a drying chamber. Sets A and B are thus divided into 5 groups of 3 samples, each group being transferred from a chamber to another.

### 3.1.3  Relative humidity selection

Various hermetic chambers with fixed $RH$ are used for applying given total suction to the clay samples. These constant humidities, imposed by mean of over saturated saline solutions, are chosen such that $s$ values are relevant to validate the retention curve in the same range as already known reference curves. After analysing the retention results from Volckaert et al. (1996) and Lima et al. (2012), 7 values of $RH$ have been chosen. The necessary salts and the theoretical $RH$ associated, at 20°C, are given in the second and third column of table 2. In a concrete way, a container filled with the saturated saline solution is placed at the bottom of each chamber.

In the laboratory conditions, notably with temperature of around 21°C and regular opening/closing of the chambers, the real measured relative humidities are presented in fourth

*Table 2: Relative humidity selection with saline solution (RH values at 20°C) (Volckaert et al. 1996), values of RH really measured and corresponding suction.*

| Chamber n° | Salt used | Theoretical $RH$ | Measured $RH$ (%) | Real $s$ (MPa) |
|---|---|---|---|---|
| 1 | $K_2SO_4$ | 97 | 96 | 5 |
| 2 | $ZnSO_4$ | 90 | 92 | 11 |
| 3 | $KCl$ | 86 | 90 | 14 |
| 4 | $NaCl$ | 76 | 80 | 30 |
| 5 | $NH_4NO_3$ | 65 | 69 | 50 |
| 6 | $Ca(NO_3)_2$ | 55 | 60 | 69 |
| 7 | $MgCl_2$ | 33 | 38 | 131 |

161 column of table 2. The consequent total suction applied to the clay placed into the cell is given

162 in the last column of this same table.

163     In order to reduce the duration of the experiment, each group of three samples only transfers

164 across 2 or 3 chambers, the total suction range being covered by the whole set of samples.

165 **3.1.4 Data acquisition**

166 First of all, total suction $s$ and degree of saturation $Sr$ (or water content $w$) need to be known

167 to establish the retention curve (looked for both series A and B). On one hand, suction is

168 known because it is imposed in each chamber by the specific saline solution. On the other

169 hand, the current water content $w$ is obtained by weighing the samples once equilibrium is

170 reached in the material (a constant mass after various days in the chamber means equilibrium

171 is achieved) on condition that the final dry mass is also recorded.

172     In addition, for series B, the clay cylinder shape is investigated for mechanical anisotropy

173 analysis. The diameters of interest are obviously the diameters perpendicular $D_\perp$ and parallel

174 $D_\parallel$ to the bedding planes but, as previously stated, these directions are not visible in the initial

175 saturated state. Therefore, arbitrary directions of diameters, $D_1$ and $D_2$, are chosen according

176 to the mark initially made at the top of the cylinders (fig 2a). The height $H$, $D_1$ and $D_2$ are

177 thus determined at each equilibrated state by using a slide caliper. Diameters are measured at

178 the mid-height of the clay cylinders. At the end of the tests, $D_1$ and $D_2$ directions are finally

179 compared to the revealed bedding planes (fig 2b). Only the relevant measurements, those made

180 perpendicularly and parallel to the bedding planes, are conserved in the results (fig 3). For

10

series B only, degree of saturation can then be obtained thanks to the measured values of $H$, $D_\parallel$, and $D_\perp$ at each equilibrium state, from which is computed the current volume $V$ (cylinder with spherical or elliptical base). The current degree of saturation $Sr$ is computed with the expression given in equation 2.

$$Sr = \frac{w}{\rho_w}\left(\frac{m_s}{V - \frac{m_s}{\rho_s}}\right),\tag{2}$$

($m_s$ being the dry mass and $V$ the total volume).

Lastly, in order to confirm the stability of experimental conditions, temperature and hygrometer sensors are placed in each hermetic chamber.

## 3.2 Results and interpretation

### 3.2.1 Retention curve

Boom Clay retention curve has already been well investigated (Delage et al. 2007a; Lima et al. 2012; Romero et al. 1999). However, as shrinkage is studied here along successive hygro-mechanical balanced states, it is worth plotting the retention path corresponding to the volumetric strains.

For both series, the evolution of $w$ with suction has been plotted in figure 4. Values of degrees of saturation determined for samples of series B are added on the graph.

We can see that the imposed suction in each chamber is globally constant, except for chamber 1 (the most humid), where $s$ varies between 1.5 and 5 MPa.

Experimental references concerning drying path of the retention curve have been added in this graph. These literature results have been obtained using saline solutions (Delage et al. 2007a; Lima et al. 2012) and chilled-mirror dew-point psychrometer (Lima et al. 2012).

The present result slightly differs from Lima's curve realised with chilled-mirror dew-point psychrometer, but the change of saturation technique already makes appear a discrepancy in the authors' results. Besides, the retention curves from Lima et al. (2012) (for the salt solution method) and Delage et al. (2007a) are well fitted, which validates the experimental method

<sup>205</sup> here adopted.

<sup>206</sup> Finally Van Genuchten (1980) retention model fitting our data is also plotted in figure 4.

<sup>207</sup> The expression of this curve is given in equation 3 with fitting parameters $N$=2 and $A$=0.06

<sup>208</sup> MPa$^{-1}$.

$$Sr = (1 + (sA)^N)^{1/N-1} \tag{3}$$

<sup>209</sup> **3.2.2   Anisotropic shrinkage**

<sup>210</sup> For each chamber applying a specific suction, the resulting strains are computed along the

<sup>211</sup> height $H$ of the clay cylinders (direction which is parallel to the bedding planes) and along $D_\perp$

<sup>212</sup> and $D_\parallel$. Moreover, volumetric strain is computed considering a cylindrical volume with elliptic

<sup>213</sup> base defined by $H, D_\perp$ and $D_\parallel$. These four deformations are plotted in figure 5 according to

<sup>214</sup> the suction applied.

<sup>215</sup> First, it appears that shrinkage (volumetric strain) reaches between 12 and 25% depending

<sup>216</sup> on the suction applied. Discrepancy for the same $s$ can be explained by the heterogeneity of

<sup>217</sup> the clay, and imprecisions of measurements. But the main point to notice is that strains are

<sup>218</sup> significantly higher perpendicularly to the bedding planes than parallel to them, whatever the

<sup>219</sup> suction. Indeed strains in parallel to the structural planes reach 3 to 9 % while they reach 6

<sup>220</sup> to 16% in perpendicular to these planes. Figure 6 presents the evolution of the ratio $\lambda = \frac{\varepsilon_\perp}{\varepsilon_\parallel}$

<sup>221</sup> with the suction applied. It appears that $\lambda$ linearly increases with the drying but its whole

<sup>222</sup> values are around 1.5 and 2.5. This value around 2 corresponds to the anisotropy ratio between

<sup>223</sup> perpendicular and parallel moduli proposed by François et al. (2014) or Chen et al. (2011).

<sup>224</sup> Boom Clay structural anisotropy thus influences mechanical anisotropy. The orientation of the

<sup>225</sup> clay particles in parallel to the bedding planes, may be responsible for this behaviour since the

<sup>226</sup> already orientated porosity facilitates the strains normally to these planes.

<sup>227</sup> Considering a sample crossing successively all the chambers, it appears from the graph of

<sup>228</sup> fig.5 that the main part of the strain is reached for a suction lower than 5 MPa. The strain

<sup>229</sup> level still increases a little from $s$ =5 to 11 MPa but, then, almost stabilizes beyond this value.

230 According to the retention curve (fig 4), the degree of saturation is almost 100% for $s< 5$ MPa

231 and rapidly decreases between $s=5$ to 10 MPa. This means that the main amount of shrinkage

232 may corresponds to normal shrinkage (that is to say shrinkage without loss of saturation),

233 which appeared for $s< 5$ MPa.

234

235 Using a suction control method by (vapour equilibrium technique), this first campaign gives

236 access to valuable information concerning shrinkage, as its amount and its anisotropy in the

237 balanced state. However, this protocol does not analyse the evolution of shrinkage in time and

238 its propagation within the material under a fixed and unbalanced drying condition applied on

239 a boundary. Therefore, a second campaign is presented hereafter, in which convective drying

240 is imposed on one side of Boom clay samples and progressive strains are followed until the final

241 equilibrium.

# 4  Shrinkage analysis under convective drying

In this approach, shrinkage is not any more analysed for steady and uniform state of the clay. The objective is to analyse in more details the transient response obtained under convective drying solicitation.

## 4.1  Sample preparation

In order to accurately study the drying kinetics and its mechanical consequences, various samples have to be prepared and dried. They are all cut from a unique clay sample whose saturation has been realized with the following protocol.

### 4.1.1  Saturation phase

A cylindrical Boom clay sample, with diameter 36 mm, length 35 mm and bedding planes parallel to the axis, is drilled into a core from the Belgian Underground Reasearch Laboratory. To achieve a full saturation, it is submitted to water injection into a triaxial device with a confinement of 3.25 MPa and an injection pressure of 1 MPa progressively applied. The effective pressure applied on the granular skeleton thus equals 2.25 MPa at the end of the loading, that is to say the in situ effective stress value (Delage et al. 2007b), which prevents from non representative swelling during the wetting.

According to the hydraulic conductivity of this material, a water pressure gradient of 1 MPa applied in parallel to the bedding planes can theoretically lead to a full saturation after 40 days. Therefore, the degree of saturation only begins to be checked after 5 weeks within the triaxial. This control is based on Skempton's coefficient computation as detailed in the following, illustrated by fig. 7.

First, the injection system is closed upstream and downstream of the triaxial cell (fig. 7a). Then an increment of total pressure $\Delta p$ is applied to the clay sample, while the increase of interstitial pressure $\Delta u$ is measured inside the material (fig. 7b). Finally the total pressure is reduced to its initial value. The more the material is saturated, the more the ratio $\Delta u/\Delta p$, defining the theoretical Skempton's coefficient $B$, is closed to 1. This is justified by a Biot

14

268 coefficient around one for Boom Clay (Bernier et al. 2007; Gens et al. 2007). Indeed by

269 assuming the quasi incompressibility of water and grains, if the injection is closed, a stress

270 increment applied on the grain-pore system leads to a skeleton strain only induced by empty

271 pore contraction. Therefore, if all pores are filled with water, no strain can take place, because

272 of water incompressibility, and the stress is entirely transferred to the water phase.

273 In fact, as grains and water are not totally incompressible, Skempton's coefficient value

274 cannot be exactly equal to 1 but is restricted to a maximum value given by equation 4.

$$B_{max} = \frac{1}{1 + n\frac{C_w - C_s}{C - C_s}}, \tag{4}$$

275 with $C_w$ the real water compressibility, $C_s$ the grains' compressibility, and $C$ the global

276 undrained compressibility of clay.

277 Notice that the system valves and tubes also add a fictive compressibility that could impact

278 the computed value of $B$ (Bishop 1976). In consequences, in the present case, saturation is

279 assumed once B reaches 0.8. This is done after around 7 weeks, when a total stress increment

280 approximately equals 1 MPa provides a Skempton's coefficient B=0.83.

### 4.1.2   Sampling

282 Once the Boom Clay cylinder is taken off from the triaxial device, a careful cutting is realized

283 in order to optimize the material whose saturation is so time-consuming. As the drying device

284 requires few grams samples, 12 samples with a size of the order of a centimetre could be cut

285 into the saturated clay. It is planned that samples will be dried from a unique top surface. This

286 will guarantee a uniform direction of incidence of the air flow over the surface and will simplify

287 the result analysis because of the globally unidirectional transfers induced within the samples.

288 Therefore, in order to test different material depths under the drying surface, 3 sample sets

289 are prepared: 4 cylindrical samples are drilled with a height of 5 mm, 4 with a height of 10

290 mm, and 4 with a height of 15 mm. They all have a diameter of 15 mm. In addition, the

291 direction of the bedding planes, whose influence on drying is not focused on in this work, is

chosen parallel to the axis of the cylindrical samples. A scheme of the sampling is presented in figure 8a.

The 12 samples are then immersed into hot liquid paraffin, the temperature being sufficiently high to make the paraffin firmly stuck to the clay. That will prevent from the detachment of the liner during drying and thus from the expansion of the drying surface area (see a dried sample example in fig.8b). This covering also makes possible to hermetically store the samples before performing the drying test, and to easily skin the top surface for a sample about to be dried (figure 8b). Another preventive measure to avoid evaporation during the storage, is to placed all sealed samples into the saturated atmosphere of a dessicator filled with water.

Finally, the samples are numbered as follows: the first part of the number corresponds to the sample length while the second part distinguishes the 4 samples of the same dimensions. For example 5-1 is the first sample of 5 mm depth.

## 4.2   Drying protocol

The protocol has been established by several previous tests from which the most relevant and practical conditions have been determined.

### 4.2.1   Drying device

The device used for the present drying tests is a micro-convective-dryer, designed in the Laboratory of Chemical Engineering few years ago for studying many different materials as wastewater sludges, mortar cement, fruits, etc. (see for instance Léonard (2002); Bennamoun et al. (2013)). It is suited for drying samples of a few grams by a convective air flow with controlled temperature and velocity.

A simplified scheme of the device is presented in figure 9. One part of the system is dedicated to the air flow regulation with a pneumatic valve connected to a flowmeter (n°1 to 4 in fig.9). The other part of the system aims to heat the air up to the needed temperature, with a regulation system (n°5 and 6). Air flows into a 4×4 cm section cell with 15 cm length (n°9), where temperature and relative humidity are measured (n°7). The sample to be dried is placed on a support hanged under an analytical balance (n°8), sensitive to 1 mg, and its mass

16

is registered at regular time intervals. It has been verified with an independent weighing, that potential air turbulence in the drying cell has a negligible effect on this measure.

### 4.2.2   Drying conditions

The test conditions have been adopted to simulate a convective drying which could be likened to the drying conditions in galleries excavated in Boom Clay. They respect:

- a vertical position of the cylinder (it is assumed that gravity has no effect on water transfers for such fine pore size),

- an air flow as far as possible parallel to the drying surface,

- a temperature between 23.6 and 24.1 °C,

- a velocity of the flow about 0.8 m/s.

Given this temperature, the ambient humidity in the laboratory during the tests and the compressed air system, which is necessary to impose the air flow but dries the air, the resultant relative humidity $RH$ measured in the drying cell ranges between 3.2 and 3.4%. This value is very low, meaning that the drying imposed in the present experiment is quite intense.

### 4.2.3   Data acquisition with X-ray micro-tomography

In addition to the samples' weighing (every minute in the present case), the 3D geometry and the internal organization of each drying sample are analysed at regular steps of the tests by mean of micro-tomography method.

The technique used for that non-destructive investigation is based on X-ray radiations. It lies on the property of each material to attenuate X-rays with a specific coefficient $\mu$ (in m$^{-1}$) which depends on the atomic number $Z$, the electronic density $\rho$ and the photon energy $E$ according to Vinegar and Wellington (1987):

$$\mu = \rho \left( a + \frac{bZ^{3.8}}{E^{3.2}} \right), \tag{5}$$

17

where $a$ depends on the photon energy and $b$ is a constant empirically determined (Vinegar and Wellington 1987). The object under study is scanned with different angles of X-ray radiation, each orientation leading to a global view of the resulting attenuation coefficient for the whole matter crossed. The whole set of these images, called 'projections', can be post-treated to obtain views of the material cross section.

For this experimental campaign, the device used is a Skyscan-1172 scanner (Skyscan, Belgium). The scanning frequency during the drying is initially fixed to 50 min but, after some tests, it has been adapted to better fit the first part of the kinetics during which evaporation goes fast. For samples 10-3, 10-4, 15-3 and 15-4, scanning is thus led at 15, 30, 45, 60, 90, 150 and 210 minutes. All samples are also scanned in the saturated and dry states. For each scan, the samples are taken off the dryer, covered, and put into the tomography apparatus. The chosen image pixel size is 34.63 $\mu$m or 31.86 $\mu$m. Such precision is accurate enough and, in the same time, limits the scan duration to 7-8 min, which prevents evaporation while the drying test is suspended. The samples weighing before and after the scan, indeed shows that less than 1% of the mass is lost during this phase. This short disruption of the drying tests also limits the redistribution of moisture within the samples.

## 4.3    Tomography post treatment

An example of scanning projection is visible in figure 10a for a 5 mm height sample (sample 5-2). It can be noticed that the paraffin cover has only a very light color, due to its low density. The first treatment to lead is cross section reconstruction, which is done along the dotted line direction indicated on the figure.

### 4.3.1    Reconstruction

'Reconstruction' process consists in applying mathematical treatments to the projection images for extracting the attenuation coefficient of each internal point and, by this way, getting cross section images of the analysed sample. In the present case, the cross sections are obtained along the axis of the cylinder (which corresponds to the global direction of the water transfer). Examples of unprocessed reconstructions are presented in figures 10b.

18

### 4.3.2  Image analysis

The cross section images along the clay sample make possible to follow various geometrical characteristics (volume, cracks, etc.), although only shrinkage is focused on in this paper. To quantify this last, it is necessary to determine in each section the extent of the clay, without considering the empty surface covered by cracks and the light layer of paraffin around the clay cylinder. This requires to have a clear criterion to distinguish 'clay' and 'non-clay' surface. Therefore, a series of morphological operations is applied to each cross section, with Matlab image analysis toolbox. These operations, applied as an example to a given section of sample 5-2 (fig.10), are the following.

In a first stage, the image is binarized. Figure 10b presents the initial image where the paraffin jacket is slightly visible. A first binary image (fig.10c) is obtained with Otsu thresholding method (Otsu 1975), which is based on the minimization of the intra-class variance between the two sets of pixels. Then, small inclusions (coming from acquisition imperfections or from the binarization threshold) are filled (fig.10d). 'Small inclusions' are here defined by clusters made by less than 50 connected pixels

The main issue with this image processing is to both exclude irrelevant zones of the image (scanning artefacts within the cross sections, paraffin layer around the sample) and conserve as much as possible the pattern and the area covered by cracks.

This image analysis is automatically repeated for each cross section of each sample, and for every scan.

## 4.4  Results and interpretation

Because 2 samples (5-3 and 10-2) were damaged when prepared, only 10 of them were dried and analysed. The first point investigated here is the drying kinetics, necessary to later analyse the shrinkage propagation.

### 4.4.1 Drying kinetics

The mass evolution in time presented in figure 11 for sample 5-2 shows that the dry state is reached after 1 day with a strong evaporation during the first 2 or 3 hours of the test. This has been confirmed for all other 5 mm height samples. For 10 mm and 15 mm samples, dry state is attained after 2 to 3 days and 4 days respectively (not presented here).

The evaporation flux $q$ related to the drying surface $S$ can be computed from the mass loss as follows:

$$q = -\frac{dm}{dt}\frac{1}{S} \tag{6}$$

$q$ plotted along the decrease of water content $w$ (on a dry basis) is a classical curve in drying field, called 'Krischer's curve'. For sample 5-2, it gives the graph presented in figure 12a, when considering, in a first assumption, a constant evaporation surface during the test. In this figure, the rough curve presents heavy fluctuations which are due to the small time step between two weighing, during which a variation of mass is not necessarily recorded. Consequently, the curve has been smoothed with Lanczos filter (Lanczos 1956). In this method, the mass derivative at a given time $t$ is expressed from a given range of data defined from $(t - n.dt)$ to $(t + n.dt)$, $n$ being called the 'semi-length filter' and $dt$ being the time between two measures. More details on this procedure are given for instance in Léonard (2002). The smoothed resulting curve with a semi length filter ('SLF') equal to 6 is visible in the same figure 12a.

Since clay may undergo shrinkage, the assumption of a constant drying area cannot be conserved and a correction of the Krischer's curve is necessary. Following Léonard et al. (2002) and May and Perré (2002), tomography is used to get the real drying surface and to correct the flux $q$. The top section area of the clay cylinders is then extracted from the image analysis, assuming that internal surface of cracks does not contribute to increase the drying surface. Indeed, given their very thin opening (less than 0.7 mm), it can reasonably be considered that they are submitted to a relative humidity close to 100%. This computation provides, after linear extrapolation, the surface evolution shown in fig. 12c. This plot gives a first idea of the

20

shrinkage evolution, which appears concentrated in the first stage of the test. The corrected Krischer 's curves (with and without smoothing) are finally presented in fig. 12b.

This process better reveals a first stage during which the evaporation rate slightly varies. Indeed, plotting the tangent to the drying curves for the initial water content makes appear a lower initial slope for the updated drying surface (fig.12b) than for the constant surface (fig.12a). This quasi constant drying rate lasts up to a water content around 0.2. Afterwards, $q$ decreases more intensely. Such stages can be assimilated to classical 'Constant Rate Period' (CRP) and 'Falling Rate Period' (FRP) of drying kinetics (Sherwood 1929a,b). It is admitted that, during CRP, the evaporation flux is limited by external factors, being temperature and relative humidity which remain constant along convective drying tests due to the air renewal. Then, during FRP, evaporation at the drying surface becomes faster than the water transfer within the material. The kinetics thus becomes controlled by internal factors being the transfer of water up to the drying surface.

Corrected Krischer's curves for the 10 dried samples are plotted in fig. 13a, b, c. First of all, the water contents pointed out for the scans of sample 5-2 (arrows in fig.13a) show that the drying disruption has no visible effect on the drying rate. It means that no significant moisture redistribution occurs during the scanning. Below each of these graphs is plotted the derivative of the drying flux $q$ with respect to the water content $w$ during the first stage of the tests (fig.13d, e, f). This makes possible to determine when the variation of the flux emphasizes, that is to say when transition between CRP and FRP can be considered. This transition is arbitrarily fixed for $dq/dw$ equal to $2.10^{-3}$ kg/m$^2$/s, which makes possible to give $w$ for sample 5-1, 5-2, 5-4, 10-3, 10-4. For Krischer's curve of sample 10-1, the initial derived of $q$ is not even lower than $2.10^{-3}$ kg/m$^2$/s, but it starts to hardly increase at $w$ close to 0.22. No transition can be caught from fig.13 f concerning samples of 15 mm high. However, it could be estimated for samples 15-1 and 15-3 from the rough curves. Finally, only samples 15-2 and 15-4 present a decreasing flux. Overall, fig.13 makes appear that the longer the samples, the less visible the CRP is (plots a, b and c) and the stronger the decrease of the flux along the loss of water content is (plots d, e and f). This may be due to internal limitation increase when enlarging the porous layer to be crossed by water before reaching the drying surface. Such influence of

the dimensions has been focused on for other kind of rocks (Prime et al. 2015).

The values of $w$ at the CRP/FRP transition are gathered in table 3, together with the time at which the transition occurred (deduced from the critical water content).

According to these data, it appears that the Constant Rate Period lasts a very short time, which is consistent with the high internal limitations expected for such a low permeable material. Beside, it can be noticed that the water content at this stage is about 0.18 whatever the duration of the CRP. Although this value stands for the mean water content over each sample, it can be related to the retention curve obtained in fig.4. It appears that $w$=0.18 corresponds to a degree of saturation not far from 100 % and to the range of suction from which the shrinkage has been observed to stabilize (fig.5).

*Table 3: Elapsed time and water content at the end of the CRP*

|          | 5-1  | 5-2  | 5-4  | 10-1 | 10-3 | 10-4 | 15-1 | 15-2 | 15-3 | 15-4 |
|----------|------|------|------|------|------|------|------|------|------|------|
| $t$ [min] | 30   | 60   | 45   | 45   | 60   | 60   | 70   |      | 50   |      |
| $w$ [-]   | 0.17 | 0.18 | 0.19 | 0.22 | 0.18 | 0.18 | 0.20 |      | 0.19 |      |

From the CRP flux values, mass and heat convective transfer coefficients, $\alpha$ and $\beta$ respectively, can be computed. They give valuable information because they quantify the intensity of convective transfers for each drying test. According to the limit layer model (illustrated in figure 14), water and heat transfer fluxes during CRP are ruled by diffusion mechanism at the drying surface. On one hand, water transfer is proportional to the difference of water content between the wetted surface and the environment expressed, in this work, as a vapour density potential (as proposed by Ben Nasrallah and Pere 1988) where $\alpha$ represents the proportionality coefficient. On the other hand, one part of the heat transfer is proportional to temperature driving potential with $\beta$ proportionality coefficient, while the other part depends on the amount of evaporated water. CRP water and heat fluxes, $q_{cst}$ and $q_h$ respectively, can thus be expressed as follows (Ben Nasrallah and Pere 1988):

$$q_{cst} = \alpha(\rho_{v,sat} - \rho_{v,air})(kg/m^2/s) \tag{7}$$

$$q_h = \beta(T_{air} - T_h) - Lq_{cst}, (W/m^2) \tag{8}$$

where $\rho_{v,sat}$ and $\rho_{v,air}$ being respectively the vapour density on the surface of the porous material and in the surrounding air, $T_h$ and $T_{air}$ being respectively the temperature (in K) on the surface and in the air, and $L$ the latent heat of water.

During the CRP, water vapour is supposed to saturate the surface of the sample ($\rho_v = \rho_{v,sat}$), and the surface temperature is assumed to correspond to the wet bulb temperature, that is to say the temperature for a relative humidity equal to 100% ($T = T_h$). Besides, it is supposed that the heat supplied to the system is only consumed to evaporate the water film. In other words, no heat is transferred to the sample itself. $\alpha$ and $\beta$ can thus be obtained as follows:

$$\alpha = \frac{q_{cst}}{(\rho_{v,sat} - \rho_{v,air})}(m/s) \tag{9}$$

$$\beta = \frac{Lq_{cst}}{(T_{air} - T_h)}, (W/m^2/K) \tag{10}$$

In these expressions, the wet bulb temperature $T_h$, is calculated thanks to its relation with ambient vapour pressure $P_v$, saturated vapour pressure $P_{v,sat}$ and $T_{air}$ (Nadeau and Puigalli 1995). $P_{v,sat}$ can be determined thanks to Garrels and Christ's empirical expression (Garrels et al. 1965) for temperature between 273 and 303 K and $P_v$ thanks to the relative humidity $RH$ given that, by definition: $RH = P_v/P_{v,sat}$. Finally, densities $\rho_{v,air}$ and $\rho_{v,sat}$ can be deduced from $P_v$ and $P_{v,sat}$, with the ideal gas law.

Transfer coefficients for each test are presented in table 4. The values are quite homogeneous, with mean $\alpha$ equal to 0.051 m/s, mean $\beta$ equal to 57 W/m²/K and standard deviations lower than 10 % for both coefficients. These results are consistent with those obtained by Gerard et al. (2010). Indeed, for Boom Clay convective drying with air flow velocity equal to 1 m/s, temperature between 17 and 70°C and relative humidity between 1 and 50% , mass and heat transfer coefficients were ranging between 0.035 – 0.050 m/s and 37 and 55 W/m²/K respectively.

*Table 4: Water and heat transfer coefficients ($\alpha$ and $\beta$ respectively)*

|  | 5-1 | 5-2 | 5-4 | 10-1 | 10-3 | 10-4 | 15-1 | 15-2 | 15-3 | 15-4 |
|---|---|---|---|---|---|---|---|---|---|---|
| $\alpha$ [m/s] | 0.047 | 0.049 | 0.048 | 0.057 | 0.045 | 0.046 | 0.058 | 0.058 | 0.052 | 0.051 |
| $\beta$ [W/m$^2$/K] | 52.2 | 55.2 | 53.3 | 64.2 | 50.3 | 51.7 | 63.7 | 64.8 | 57.7 | 56.6 |

### 4.4.2    Normal shrinkage of the whole samples

Integrating the area covered by clay over all cross sections at a given time gives the volume of the scanned sample, as stated by equation 11.

$$V(t) = \sum_{k=1}^{N} S_k(t).l, \tag{11}$$

with $V(t)$ the volume of a given sample at time $t$, $N$ the number of reconstructions over the sample height, $S_k$ the area covered by the sample for the $k^{th}$ reconstruction and $l$ the distance between two reconstructions. $S_k$ only takes into account the area occupied by clay without considering the area occupied by cracks.

This makes possible to follow the shrinkage evolution along drying.

Figure 15 presents, for all samples, the evolution of the shrinkage volume (difference between initial and current volumes) along the decreasing water content. This last variable is a mean value for each sample, since moisture distribution is not uniform along the material.

In the same axes are represented the evaporated amount of water (equal to the mass loss divided by water density) along the water content, this plot being naturally linear.

From the two superposed curves of each sample, it appears that the evaporated volume equals the shrinkage volume in the first stage of the drying. Then, once the water content reaches around 0.2, the shrinkage hardly evolves with regards to the volume evaporated. This result means that early shrinkage, which represents the main part of the strain, takes place without desaturation of the clay: the water loss is counterbalanced by pore contraction. Such shrinkage is classically called 'normal shrinkage'.

To better understand this mechanism, and its link with the drying kinetics, this shrinkage

24

curve has been faced with Krischer's curve for three samples, 5-2, 10-4 and 15-1 (fig.16). Fig.16a makes appear the water content for which the desaturation starts and Fig.16b makes appear the water content for CRP/ FRP transition. These values of water content globally correspond one to another, which shows the synchronism between the mechanical and the hydraulic transition of the clay response.

Indeed it is known that internal resistances greatly increase once saturation is lost, in such a way that they can become the limiting factor with regard to the drying kinetics.

In this first analyse of the results, shrinkage evolution has been characterized in its whole, without considering the non-uniform state induced by the drying condition. Thanks to tomography, the shrinkage profile along the clay cylinders can also be investigated.

### 4.4.3   Shrinkage profile and propagation

In each cross section, the image analysis returns the area occupied by clay. The ratio between this value and the initial area of the cross section gives the relative contraction of the section which is a quantitative indicator of the shrinkage, although this ratio is only two-dimensional. Such contraction is computed for all sections in order to make appear a shrinkage profile for each time of the drying test. Moreover, plotting this profile throughout the test shows how the strains develop with the chosen drying conditions. Figure 17 illustrates this evolution for sample 10-3 (10 mm height), which has been scanned from the early stage of the drying test (15, 30, 45 and 60 min). The top-drying surface is located at the left of the curves (0 mm depth).

This figure confirms that, with the present conditions, most of the shrinkage takes place at the very beginning of the drying (around 2/3 of the final strain has developed after 1 hour). Furthermore, one can see that after 15 min, the shrinkage exhibits a globally linear repartition along the depth of the clay, with a maximum amplitude located at the drying surface while, afterwards, it progressively becomes uniform through the sample. For 5 and 10 mm depth samples, the tendency is the same, with a strain gradient disappearing from 15 min. For 15 mm samples, the strain gradient is sustained longer, until 30 to 60 min.

According to the CRP end established in table 3, this gradient develops during the CRP,

and thus still corresponds to a saturated state of the clay. As the shrinkage is normal in this period, the shrinkage amount corresponds to the decrease of water content. Therefore, it can reasonably be assumed that the water content profile also follows a globally linear repartition until 15 min for 5 and 10 mm depth samples or 30-60 min for 15 mm samples.

Such shrinkage and water content gradients correspond to conditions of 'constrained strains' and 'moisture gradient' which, according to Peron et al. (2009), are responsible for cracking.

That statement well fits our results since cracks indeed develop from the beginning of all tests performed here, included during the CRP. More experimental results about Boom Clay cracking under drying conditions can be found in Prime et al. (2014).

### 4.4.4 Shrinkage anisotropy at equilibrium

It appears that for many samples the dry cross sections are not circular but slightly elliptic.In order to orientate this strain anisotropy with regard to the structural anisotropy of the clay, it is necessary to locate the bedding planes in the final dry state. It must be reminded that samples have been drilled such that bedding planes are parallel to the axis of the clay cylinders. From the vertical cracking pattern shown as an example at fig.18 for four dried samples, it can be reasonably assumed that crack global direction follows the bedding planes. This 3D view has been obtained by assembling, for each sample, all the reconstructed cross sections.

It is thus possible to align each dry cross section with the bedding plane direction. In the saturated state, there is less need for orientating the sections since the cylinder basis is almost circular. However, the spotting of some small defaults in the clay makes possible to place the section with regards to the dry one.

Fig.19a illustrates this positioning of the saturated and dry top sections (sample 5-2) thanks to irregularities pointed out within the clay. On this figure the elliptic shape of the sample at the end of the test also appears.

Top cross sections are arbitrarily chosen to quantify this anisotropy, assuming that, at the end of the drying, strain anisotropy is homogeneous along the depth of the clay cylinder. For each sample, dry and saturated dimensions are to compare, by distinguishing parallel and perpendicular directions of diameters (denoted $D_\parallel$ and $D_\perp$ respectively) with respect to the

26

568 bedding planes. To do so, a rectangular frame is placed around the section to analyse and it

569 is orientated toward the bedding planes (fig.19a). Length and width of the rectangle are then

570 determined by imaging tools for saturated and dry state. In addition, the vertical dimensions

571 of the sample (that is to say the second direction parallel to the bedding planes) is determined

572 before and after drying in the same way, from radio analysis. Figure 19b shows for instance the

573 saturated and dry radios for the same sample 5-2. The strains for the 3 directions are finally

574 reported in figure 20. The volumetric strain (that is to say the shrinkage), determined from

575 the cross section area integration along the depth, is also plotted there.

576 First, this graph highlights that the volumetric strain reaches a final value between 14.5 and

577 25.2% (mean value equal to 18%). Except for sample 5-2, characterized by a particularly high

578 initial water content and a consequent high shrinkage, this value does not vary a lot between

579 one sample to another, with a standard deviation of 1.3% (without considering sample 5.2).

580 This result well confirms the order of magnitude of volumetric strain found in section 3 with

581 vapour equilibrium technique, which was between 12 and 25%

582 This graph also puts in evidence a clear difference between the strains perpendicular to

583 the direction of bedding planes (denoted direction $D_\perp$) with a mean value of $\varepsilon_\perp$=7.5 %, and

584 the strains in the direction parallel to them (denoted $D_\parallel$), with a mean value of $\varepsilon_\parallel$=3.75 %.

585 Bedded structure, already responsible for permeability anisotropy, is thus also responsible for

586 strain anisotropy with a ratio $\frac{\varepsilon_\perp}{\varepsilon_\parallel}$ equal to 2. This value is consistent with the anisotropy ratio

587 found in section 3 which ranged between 1.5 and 2.5 depending on the suction applied.

588

# 5 Conclusion

The two experimental campaigns presented in this paper both aimed to characterize the Boom clay shrinkage. Both simple measurements (as dimension measures, weighing, etc.) as well as high tech methods (X-ray micro-tomography, automatic image processing) have been used to this end.

The first proposed campaign refers to vapour equilibrium technique for which increasing values of relative humidity are applied and total suction varies between 5 and 140 MPa. All states analysed are steady states. On the contrary, the second proposed campaign refers to a convective drying during which clay response is followed until reaching equilibrium. Because of a low and constant ambient relative humidity (about 3%), suction in this case corresponds to a value around 480 MPa, which means that drying conditions are stronger. Despite their strong differences, these two experimental methods lead to very similar results concerning shrinkage in the balanced state. First, the final shrinkage is about 18% with convective drying while it reaches a mean value of 18.5% with vapour equilibrium technique for the higher values of suction, which are the closest to the convective drying conditions (suction greater than 50 MPa). Besides, both campaign make possible to determine a ratio of 2 between the strains in parallel and in perpendicular directions to the bedding planes. This is consistent with the mechanical modulus ratio found in the literature. Finally, according to both of them, the main amount of shrinkage is reached with a saturated state, which corresponds to a normal shrinkage. Vapour equilibrium technique shows that this last occurs until suction about 5-10 MPa. In addition to these consistent results, convective drying campaign makes it possible to get further information concerning the drying transient states. First of all, drying kinetics could be characterized. Notably a phasing between a quasi constant drying rate period (CRP) and a decreasing rate period (FRP) could be put in evidence, and transfer parameters could be determined. Normal shrinkage was shown to take place during the CRP. This second campaign also provides the pattern of strain propagation within the Boom Clay, which exhibits a gradient along the depth during a very early period and then becomes uniform from the evaporation surface to the core of the material.

Finally, the mechanism investigated in this study can be useful to better interpret the

28

618 transient behaviour of geomaterials under drying which is of interest in many cases (clay liner

619 for waste storage facilities, clay tiles and ceramic industry, etc.). In addition, it represents a

620 useful reference for future numerical studies aiming to model drying induced strains in Boom

621 Clay. Concerning the mechanical response of soft material under drying, many questions

622 remain open and still need to be further investigated. First of all, the water transfer pattern

623 within the material is particularly interesting since it would lead to a better understanding of

624 the physical mechanisms of water migration. Such an approach has been led for example by

625 Prime et al. (2015) on a rigid limestone by mean of micro-tomography. Another wide direction

626 to investigate concerns crack onset and development, its eventual preferential direction, its link

627 with shrinkage and with drying conditions.

# References

Aertsens, M., Wemaere, I., and Wouters, L. Spatial variability of transport parameters in the boom clay. *Applied Clay Science*, 26(1):37–45, 2004.

Alonso, E. E., Gens, A., and Josa, A. A constitutive model for partially saturated soils. *Géotechnique*, 40(3):405–430, 1990.

Alves, C., Sequeira Braga, M., and Hammecker, C. Water transfer and decay of granitic stones in monuments. *Comptes rendus de l'Académie des sciences. Série 2. Sciences de la terre et des planètes*, 323(5):397–402, 1996.

Amarasiri, A. L., Kodikara, J. K., and Costa, S. Numerical modelling of desiccation cracking. *International Journal for Numerical and Analytical Methods in Geomechanics*, 35(1):82–96, 2011.

Banaszak, J. and Kowalski, S. Theoretical and experimental analysis of stresses and fractures in clay like materials during drying. *Chemical Engineering and Processing: Process Intensification*, 44(4):497–503, 2005.

Bastiaens, W., Bernier, F., and Li, X. L. Selfrac: experiments and conclusions on fracturing, self-healing and self-sealing processes in clays. *Physics and Chemistry of the Earth, Parts A/B/C*, 32(8):600–615, 2007.

Ben Nasrallah, S. and Pere, P. Detailed study of a model of heat and moass transfer durin convective drying of porous media. *International Journal of Heat and Mass Transfer*, 31 (5): 957–967, 1988.

Bennamoun, L., Kahlerras, L., Michel, F., Courard, L., Salmon, T., Fraikin, L., Belhamri, A., and Léonard, A. Determination of moisture diffusivity during drying of mortar cement: Experimental and modeling study. *International Journal of Energy Engineering*, 3(1):1–6, 2013.

Bernier, F., Li, X. L., and Bastiaens, W. Twenty-five years' geotechnical observation and testing in the tertiary boom clay formation. *Géotechnique*, 57(2):229–237, 2007.

30

654  Bishop, A. The influence of system compressibility on the observed pore-pressure response to
655  an undrained change in stress in saturated rock. *Géotechnique*, 26(Analytic), 1976.

656  Blatz, J. A., Cui, Y.-J., and Oldecop, L. Vapour equilibrium and osmotic technique for suction
657  control. In *Laboratory and Field Testing of Unsaturated Soils*, pages 49–61. Springer, 2009.

658  Chen, G., Sillen, X., Verstricht, J., and Li, X. L. Atlas iii in situ heating test in boom clay: Field
659  data, observation and interpretation. *Computers and Geotechnics*, 38(5):683–696, 2011.

660  Dehandschutter, B., Vandycke, S., Sintubin, M., Vandenberghe, N., and Wouters, L. Brittle
661  fractures and ductile shear bands in argillaceous sediments: interferences from oligocene
662  boom clay (belgium). *Journal of Structural Geology*, 27, 2005.

663  Delage, P., Le, T. T., Tang, A.-M., Cui, Y.-J., and Li, X.-L. Suction effects in deep boom
664  clay block samples. Technical report, Ecole Nationale des Ponts et Chaussees (CERMES,
665  Institut Navier), Paris, France ; EURIDICE Group, Mol, Belgium, 2007a.

666  Delage, P., Le, T. T., Tang, A.-M., Cui, Y.-J., and Li, X.-L. Suction effects in deep boom clay
667  block samples. *Géotechnique*, 57 (1):239–244, 2007b.

668  Fleureau, J.-M., Kheirbek-Saoud, S., Soemitro, R., and Taibi, S. Behavior of clayey soils on
669  drying-wetting paths. *Canadian geotechnical journal*, 30(2):287–296, 1993.

670  François, B., Labiouse, V., Dizier, A., Marinelli, F., Charlier, R., and Collin, F. Hollow cylinder
671  tests on boom clay: Modelling of strain localization in the anisotropic excavation damaged
672  zone. *Rock mechanics and rock engineering*, 47(1):71–86, 2014.

673  Garrels, R., Christ, C., and Solutions, M. Equilibria. *Editorial Harper & Row, New York*,
674  pages 213–233, 1965.

675  Gens, A., Vaunat, J., Garitte, B., and Wileveau, Y. In situ behaviour of a stiff layered clay
676  subject to thermal loading: observations and interpretation. *Géotechnique*, 57(2):207–228,
677  2007.

678  Gerard, P., Charlier, R., Chambon, R., and Collin, F. Influence of evaporation and seepage on
679  the convergence of a ventilated cavity. *Water resources research*, 44(5):W00C02, 2008.

Gerard, P., Léonard, A., Masekanya, J., Charlier, R., and Collin, F. Study of the soil–atmosphere moisture exchanges through convective drying tests in non-isothermal conditions. *International journal for numerical and analytical methods in geomechanics*, 34(12): 1297–1320, 2010.

Granger, L. *Comportement différé du béton dans les enceintes de centrales nucléaires: analyse et modélisation*. PhD thesis, Ecole Nationale des Ponts et Chaussées, 1995.

Hedan, S., Cosenza, P., Valle, V., Dudoignon, P., Fauchille, A.-L., and Cabrera, J. Investigation of the damage induced by desiccation and heating of tournemire argillite using digital image correlation. *International Journal of Rock Mechanics and Mining Sciences*, 51:64–75, 2012.

Kodikara, J. New framework for volumetric constitutive behaviour of compacted unsaturated soils. *Canadian Geotechnical Journal*, 49(11):1227–1243, 2012.

Lanczos, C. *Applied analysis*. Prentice-Hall, 1956.

Léonard, A. *Étude du séchage convectif de boues d'épuration-Suivi de la texture par microtomographie à rayons X*. PhD thesis, Université de Liège, 2002.

Léonard, A., Blacher, S., Marchot, P., and Crine, M. Use of X-ray microtomography to follow the convective heat drying of wastewater sludges. *Drying Technology*, 20(4-5):1053–1069, 2002.

Lima, A., Romero, E., Piña, Y., Gens, A., and Li, X.-L. Water retention properties of two deep belgian clay formations. In *Unsaturated Soils: Research and Applications*, pages 179–184. Springer, 2012.

Loret, B. and Khalili, N. An effective stress elastic–plastic model for unsaturated porous media. *Mechanics of Materials*, 34(2):97–116, 2002.

May, B. and Perré, P. The importance of considering exchange surface area reduction to exhibit a constant drying flux period in foodstuffs. *Journal of Food Engineering*, 54(4): 271–282, 2002.

32

Mertens, J., Vandenberghe, N., Wouters, L., and Sintubin, M. The origin and development of joints in the boom clay formation (rupelian) in belgium. *Geological Society, London, Special Publications*, 216(1):309–321, 2003.

Mertens, J., Bastiaens, W., and Dehandschutter, B. Characterisation of induced discontinuities in the boom clay around the underground excavations (urf, mol, belgium). *Applied Clay Science*, 26(1):413–428, 2004.

Musielak, G. and Mierzwa, D. Permanent strains in clay-like material during drying. *Drying Technology*, 27(7-8):894–902, 2009.

Musielak, G. and Sliwa, T. Numerical simulation of clay cracking due to drying. In *In proceedings of Eurodrying 2013, Paris*, 2013.

Nadeau, J. and Puigalli, J. *Detailed study of a model of heat and mass transfer during convective drying of porous media*. Lavoisier, 1995.

Nowamooz, H. and Masrouri, F. Mechanical behaviour of expansive soils after several drying and wetting cycles. *Geomechanics and Geoengineering: An International Journal*, 5(4): 213–221, 2010.

Ortiz, L., Volckaert, G., and Mallants, D. Gas generation and migration in boom clay, a potential host rock formation for nuclear waste storage. *Engineering Geology*, 64(2):287–296, 2002.

Otsu, N. A threshold selection method from gray-level histograms. *Automatica*, 11(285-296): 23–27, 1975.

Péron, H., Delenne, J.-Y., Laloui, L., and El Youssoufi, M. S. Discrete element modelling of drying shrinkage and cracking of soils. *Computers and Geotechnics*, 36(1):61–69, 2009.

Peron, H., Laloui, L., Hueckel, T., and Hu, L. B. Desiccation cracking of soils. *European Journal of Environmental and Civil Engineering*, 13(7-8):869–888, 2009.

Prime, N., Fraikin, L., Leonard, A., Charlier, R., and Levasseur, S. Experimental investigation of hydro-mechanical coupling during clay drying. In *In Proceedingsof International Drying Symposium, Lyon*, 2014.

Prime, N., Housni, Z., Fraikin, L., Léonard, A., Charlier, R., and Levasseur, S. On water transfer and hydraulic connection layer during the convective drying of rigid porous material. *Transport in porous media*, 106:47–72, 2015.

Romero, E., Gens, A., and Lloret, A. Water permeability, water retention and microstructure of unsaturated compacted boom clay. *Engineering Geology*, 54(1):117–127, 1999.

Sherwood, T. The drying of solids i. *Industrial & Engineering Chemistry*, 21(1):12–16, 1929a.

Sherwood, T. The drying of solids ii. *Industrial & Engineering Chemistry*, 21(10):976–980, 1929b.

Tang, A.-M. and Cui, Y.-J. Controlling suction by the vapour equilibrium technique at different temperatures and its application in determining the water retention properties of mx80 clay. *Canadian Geotechnical Journal*, 42(1):287–296, 2005.

Tripathy, S., Rao, K. S., and Fredlund, D. Water content-void ratio swell-shrink paths of compacted expansive soils. *Canadian Geotechnical Journal*, 39(4):938–959, 2002.

Van Genuchten, M. T. A closed-form equation for predicting the hydraulic conductivity of unsaturated soils. *Soil Science Society of America Journal*, 44(5):892–898, 1980.

Vinegar, H. and Wellington, S. Tomographic imaging of three-phase flow experiments. *Review of Scientific Instruments*, 58(1):96–107, 1987.

Volckaert, G., Bernier, F., Alonso, E., Gens, A., Samper, J., Villar, M., Martin-Martin, P., Cuevas, J., Campos, R., Thomas, H., Imbert, C., and Zingarelli, V. Thermal-hydraulic-mechanical and geochemical behaviour of the clay barrier in radioactive waste repositories (model development and validation) - final report. Technical report, European Commission, 1996.
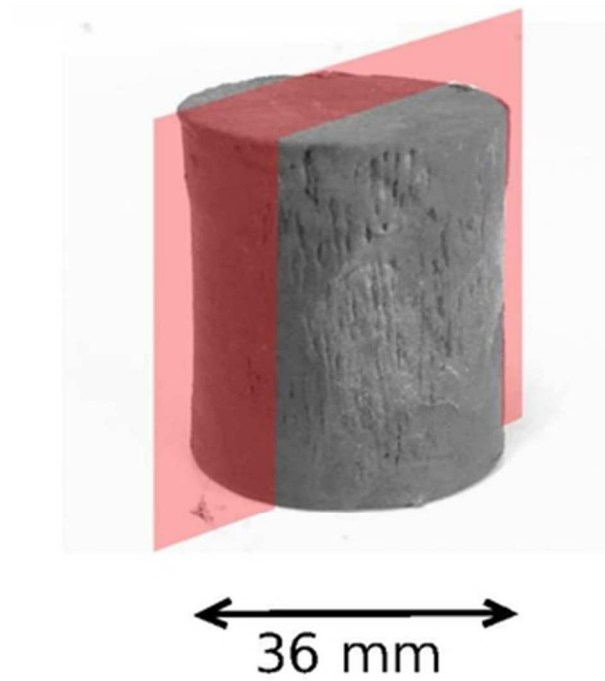
Fig.1 Visualization of bedding planes in a partially dried Boom Clay sample
26x28mm (300 x 300 DPI)
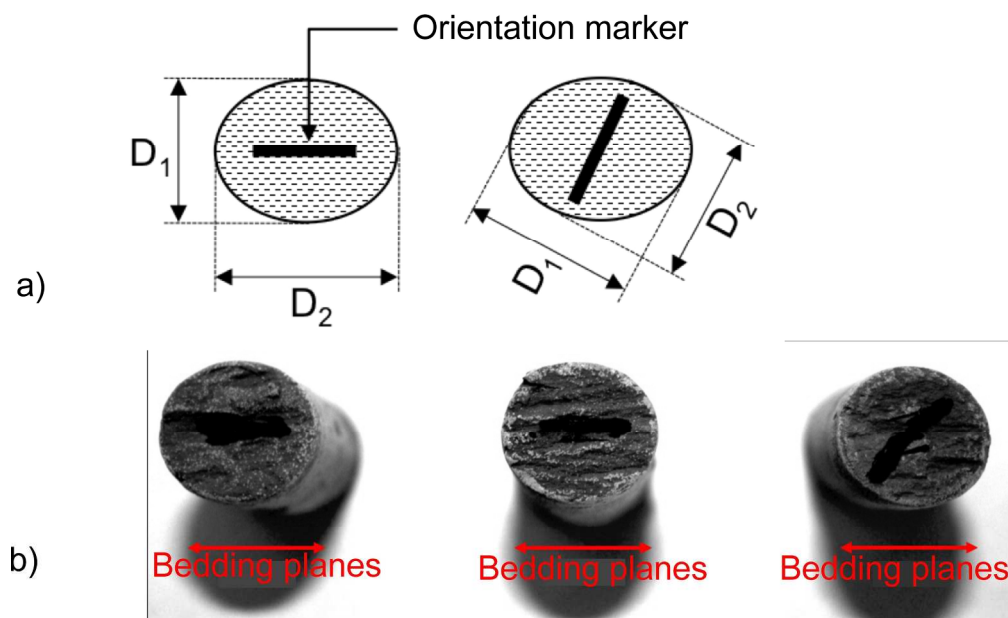
Fig.2 Measurements with respect to the marks made on the samples' surface (a) Bedding planes revealed after the drying (b)
227x152mm (300 x 300 DPI)
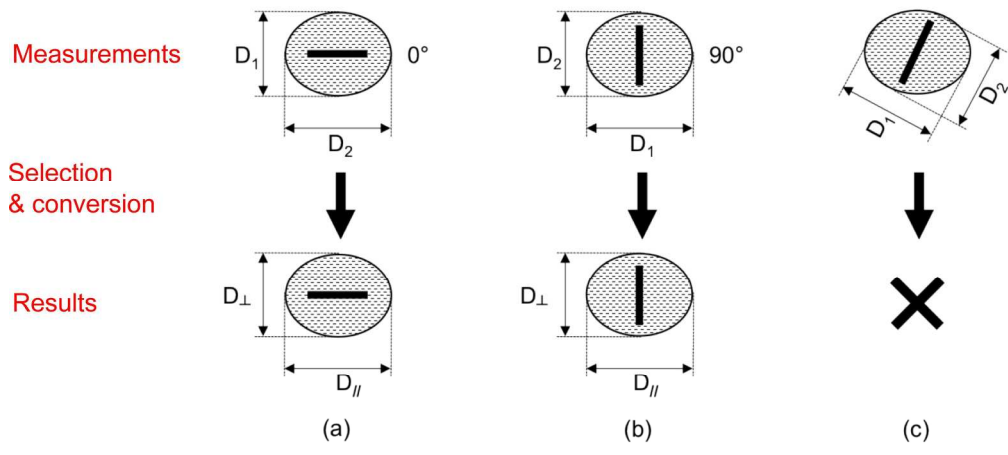
Fig.3 Determining D⊥ and D∥ from measurements
215x104mm (300 x 300 DPI)
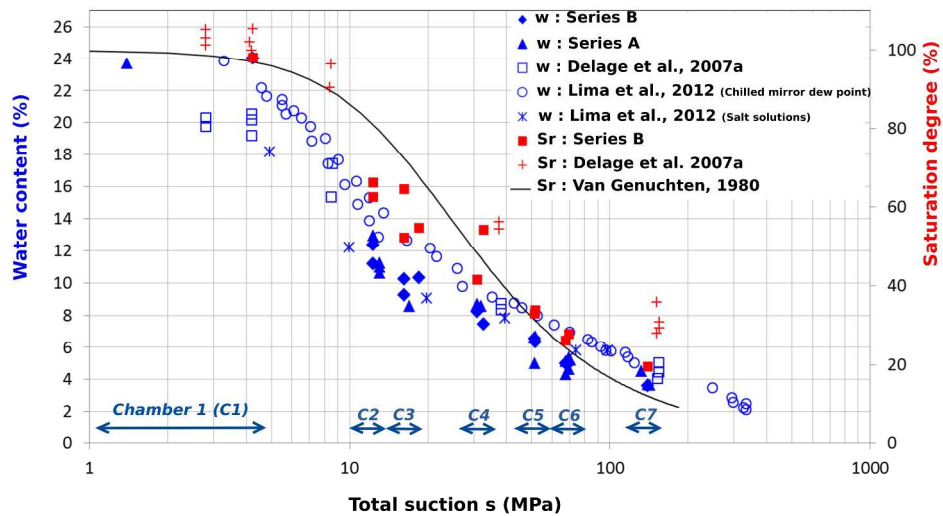
Fig.4 Drying retention path for set A and B of clay samples, plotted with water content or degree of saturation. Comparison with literature references, and with VanGenuchten (1980) model fitting the present results

308x174mm (300 x 300 DPI)
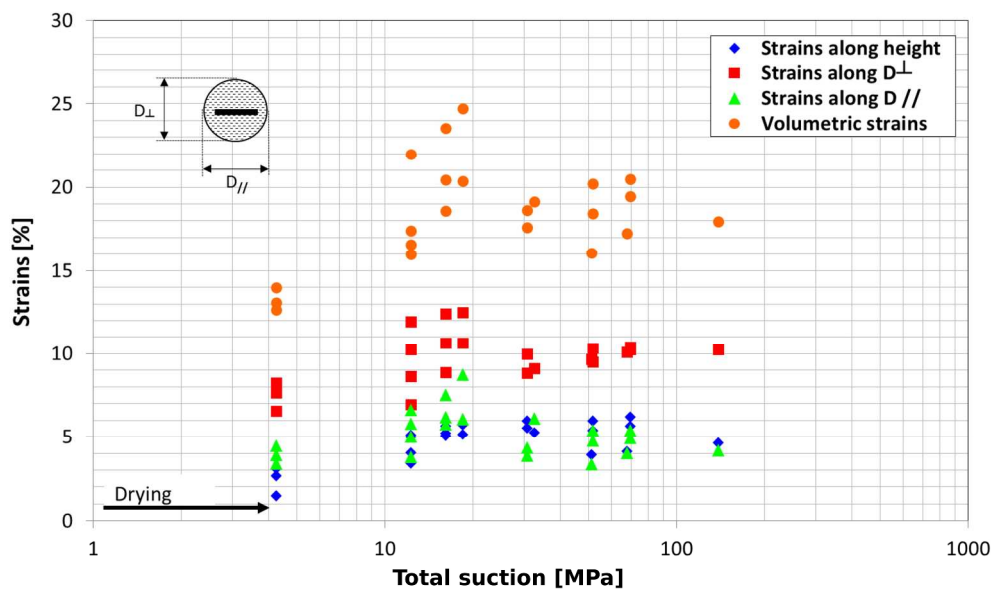
Fig.5 Synthesis of the strain anisotropy induced by drying, volumetric strain
280x183mm (300 x 300 DPI)
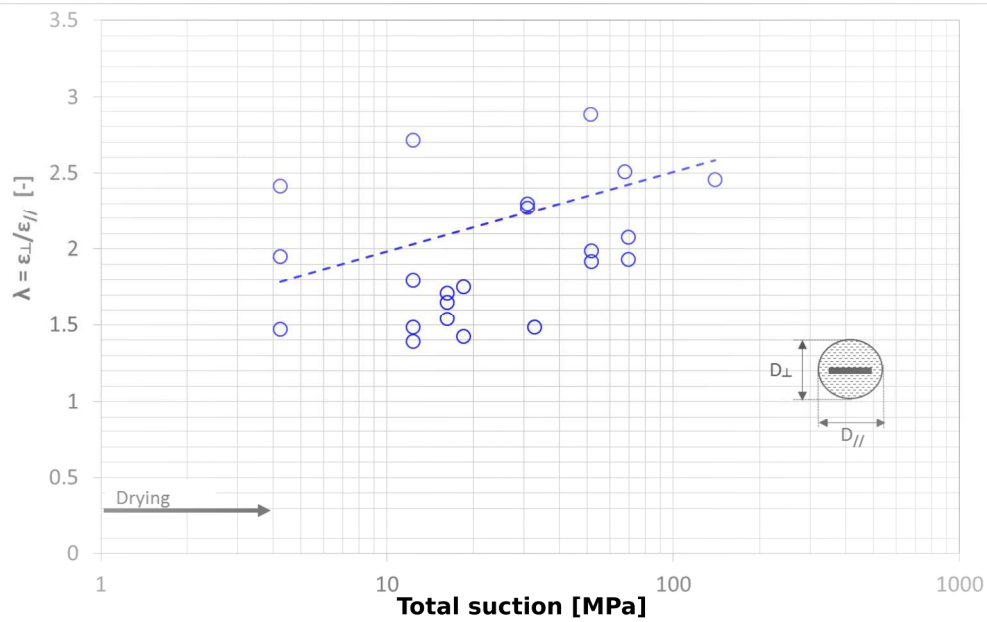
Fig.6 Evolution of ratio $\lambda = \varepsilon_\perp/\varepsilon_\parallel$ with suction
247x154mm (300 x 300 DPI)
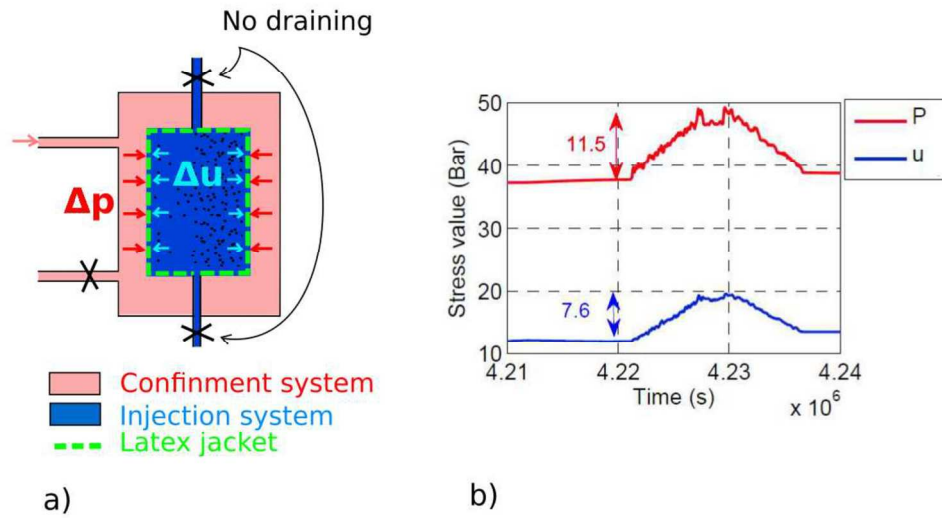
Fig.7 Saturation control within triaxial device: increment of total pressure applied (a), comparison of the total pressure p applied and the interstitial pressure u induced (here full saturation is not achieved yet) (b) 190x102mm (300 x 300 DPI)
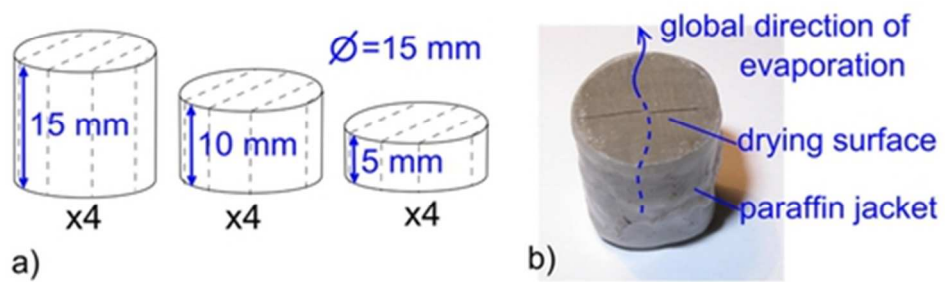
Fig.8 Samples' geometry (a) and covering (b) (Prime et al. 2014)
44x14mm (300 x 300 DPI)

1. Compressed air system
2. Pressure reducing valve
3. Pneumatic valve
4. Mass flow meter
5. Regulation
   temperature probe
6. Heating tube
7. Temperature
   and humidity probe
8. Weighting scale
9. Drying Cell
10. Dryied sample
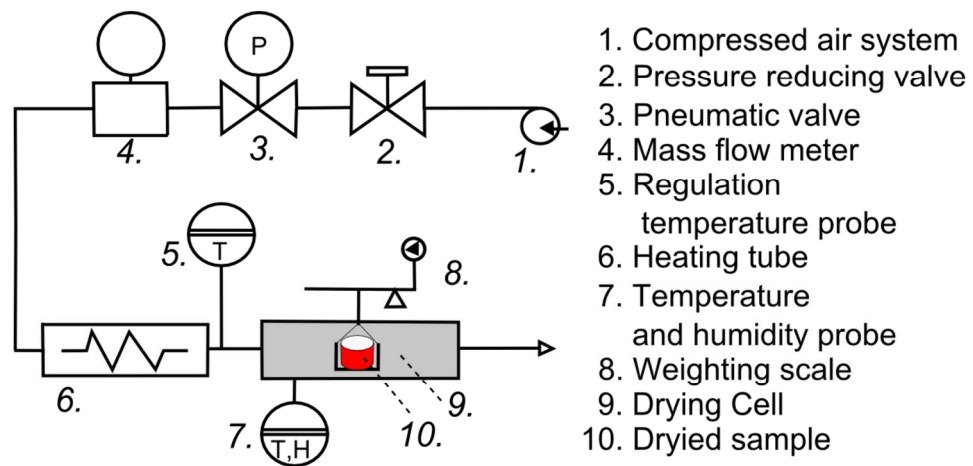
Fig. 9 Micro-drying device (Prime et al. 2014)
185x94mm (300 x 300 DPI)
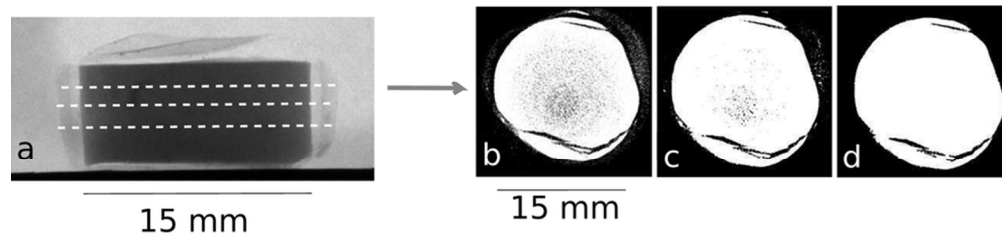
Fig.10 Image processing. Direction of reconstructed cross sections on a scanning projection of  sample 5-2
(a) Example of a rough reconstructed image (b), new image after binarisation with Otsu thresholding (c),
after small inclusions suppression (d).
83x19mm (300 x 300 DPI)
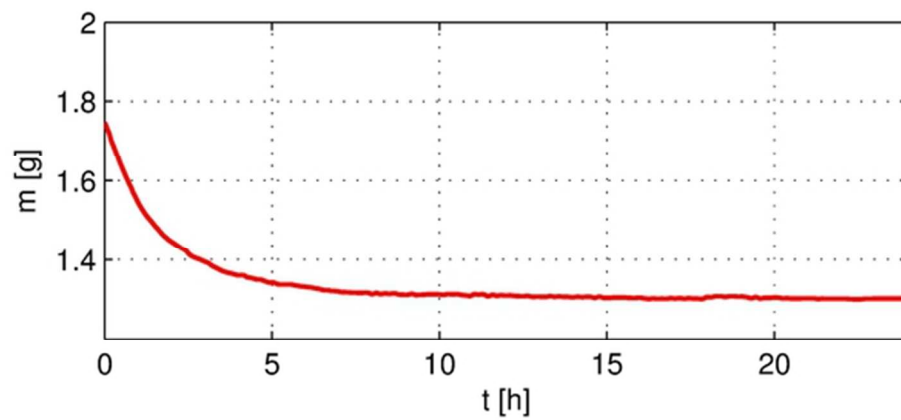
Fig.11 Mass evolution along time (sample 5-2)
55x25mm (300 x 300 DPI)
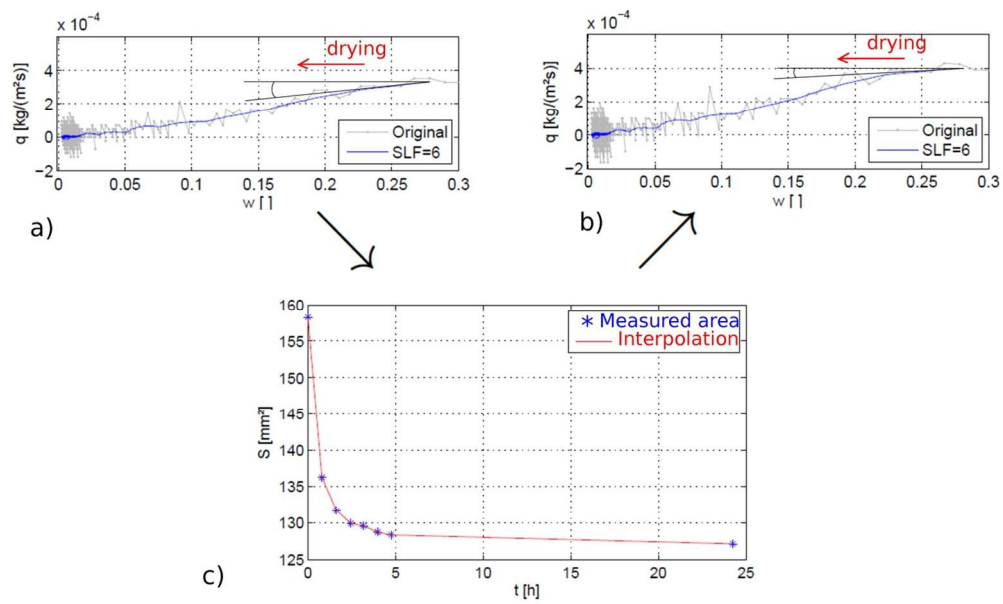
Fig. 12 Correction of drying curves with surface area update. Initial flux curve (a), corrected Krischer's curve (b), drying surface evolution along drying (c).
124x74mm (300 x 300 DPI)
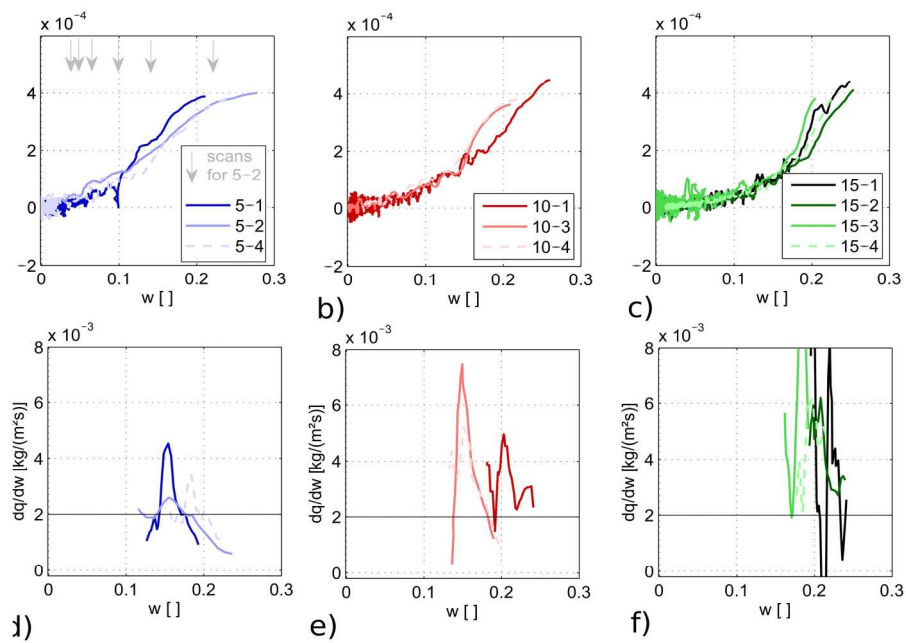
Fig.13 Krischer's curves for H=5 mm (a), 10 mm (b), 15 mm (c). Derivative of the flux dq/dw for H=5 mm (d), 10 mm (e), 15 mm (f).
199x134mm (300 x 300 DPI)
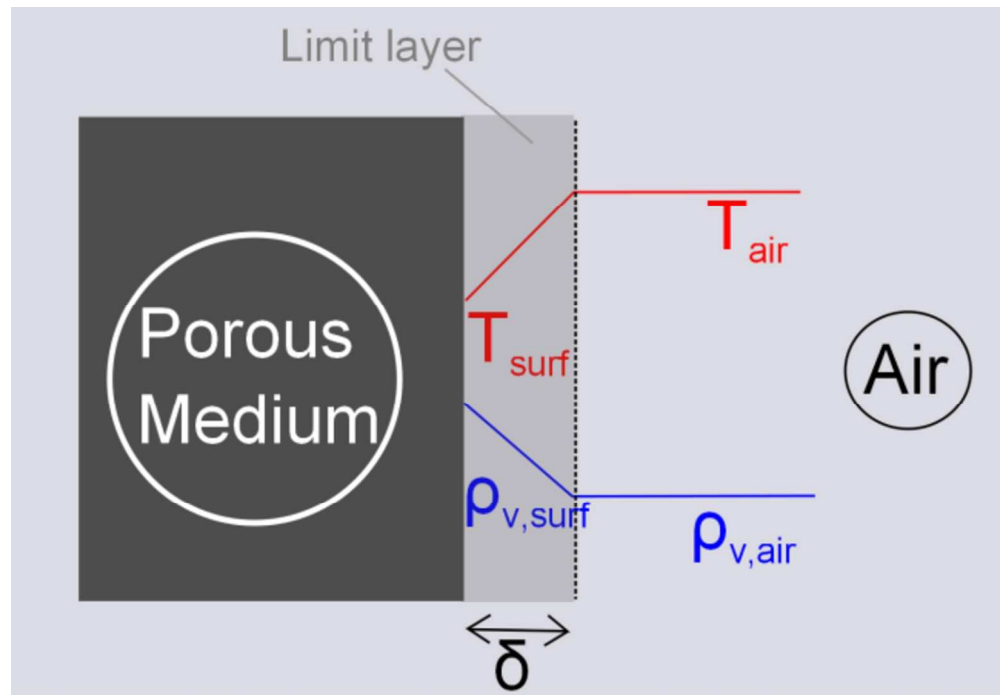
Fig.14 Limit layer model (Prime et al. 2014)
127x87mm (300 x 300 DPI)
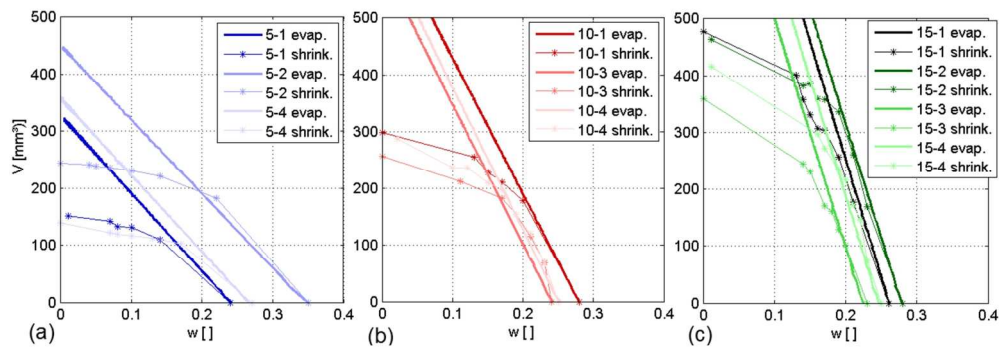
Fig.15 Evolution of the shrinkage and evaporated volumes in function of the water content for H=5 mm (a),
10 mm (b), 15 mm (c)
154x54mm (300 x 300 DPI)
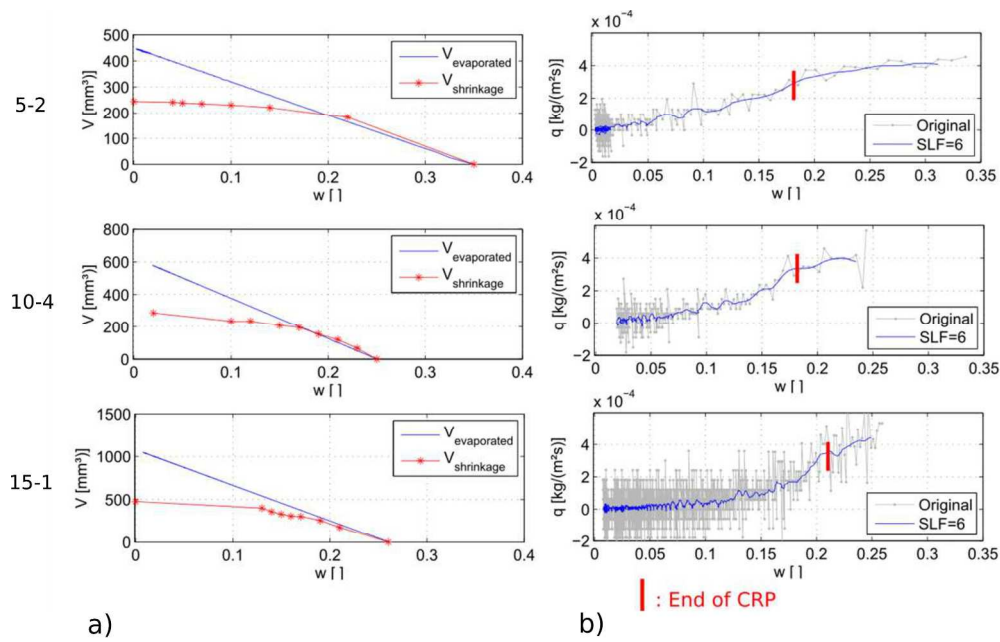
Fig.16 Synchronism between the end of normal shrinkage and the CRP end for samples 5-2, 10-4 and 15-1. Highlighting of an early normal shrinkage (a), End of the CRP, or the period with approximately constant drying flux (b).
273x171mm (300 x 300 DPI)
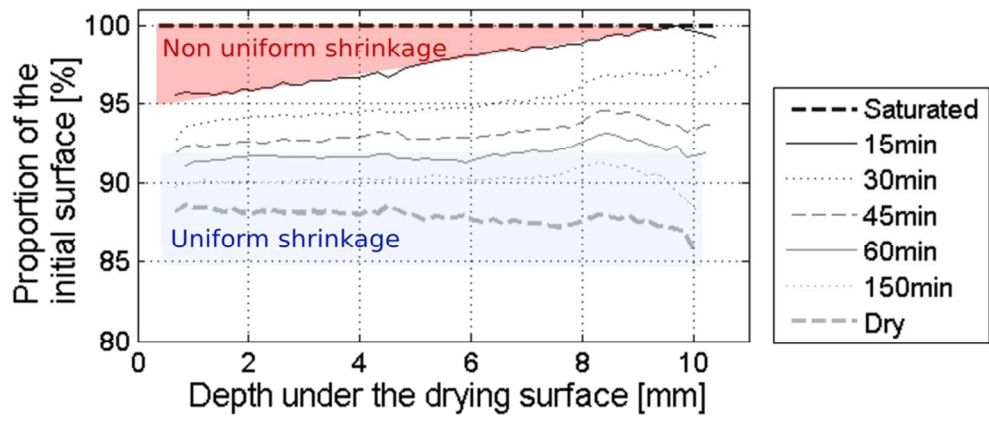
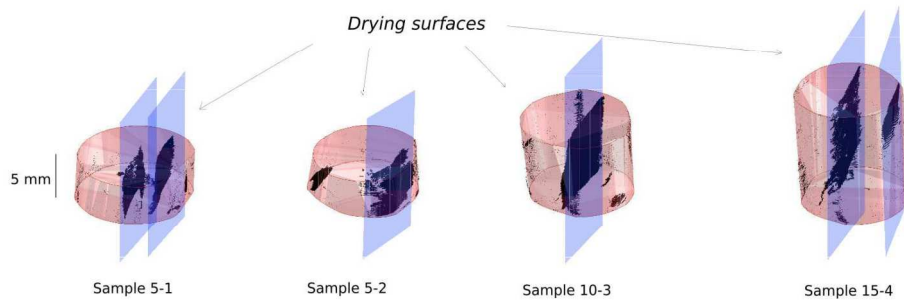Fig.17 Shrinkage propagation in sample 10-3
95x46mm (300 x 300 DPI)

Fig.18 3D view of four samples in the dry state. Cracking pattern displayed in black.
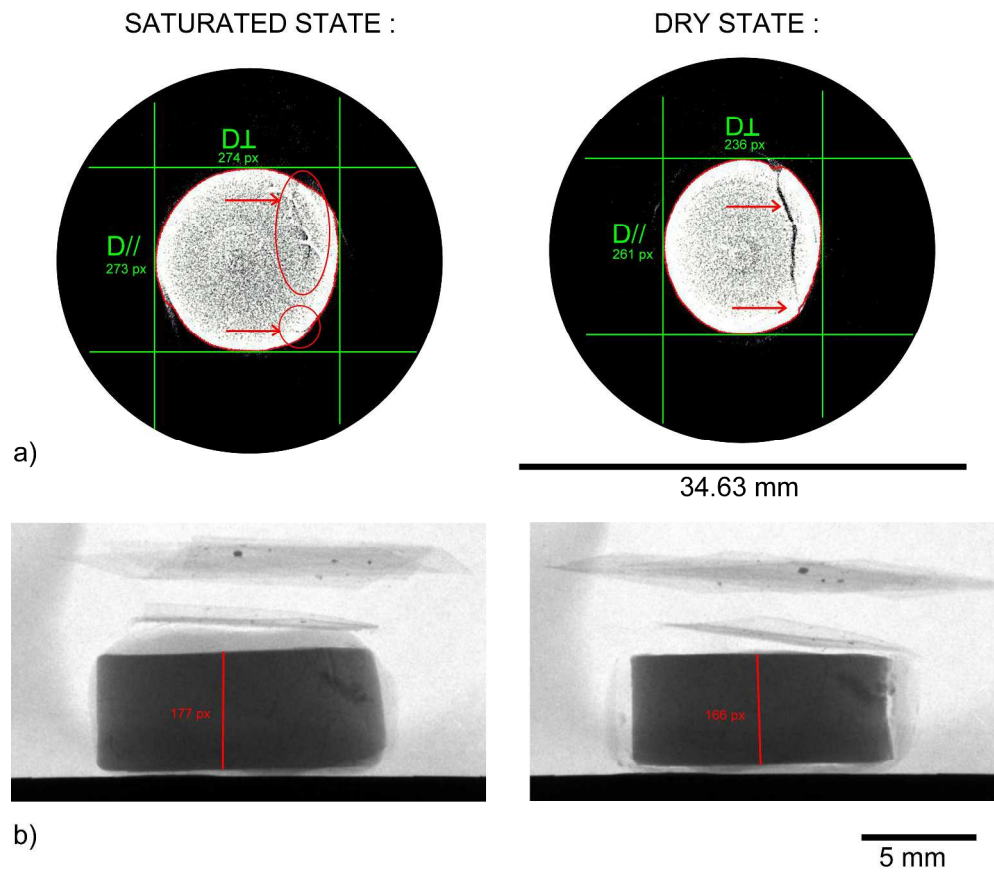1396x488mm (100 x 100 DPI)

Fig.19 Contraction of the top surface of sample 5-2 and localisation of defaults for orientating the saturated cross section with respect to dry one (a). Shrinkage of sample 5-2 along the depth (b). Dimensions are given in pixels.
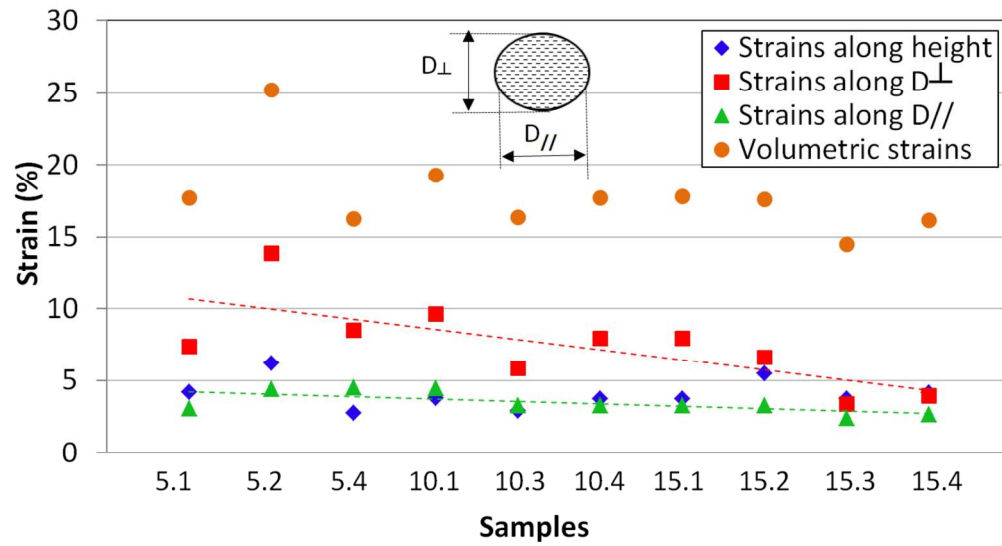359x307mm (300 x 300 DPI)

Fig.20 Final strain state for all samples: strain components along the three directions of the space and volumetric one.
258x140mm (300 x 300 DPI)